Enhanced Second-Order Nonlinearities at Strained Ultrasharp Zigzag Edges in Multilayer MoS2

THE JOURNAL OF PHYSICAL CHEMISTRY C
A JOURNAL OF THE AMERICAN CHEMICAL SOCIETY

pubs.acs.org/JPCC

Article

Enhanced Second-Order Nonlinearities at Strained Ultrasharp Zigzag Edges in Multilayer MoS_2

Adrián Dewambrechies,[‖] Alexander Yu. Polyakov,[‖] Betül Küçüköz, and Timur O. Shegai*

Cite This: *J. Phys. Chem. C* 2023, 127, 15395−15405

Read Online

ACCESS | Metrics & More | Article Recommendations | Supporting Information

ABSTRACT: Transition metal dichalcogenide (TMD) materials attract significant research attention thanks to their exceptional excitonic and optical properties. In this work, we analyze the formation of strained ultrasharp zigzag edges in MoS_2 multilayers produced by anisotropic wet etching. The topography of the edges is determined by the relative stability of the different crystallographic directions of the multilayer as well as the interlayer interactions. Furthermore, we study the linear (Raman) and nonlinear (second-harmonic generation) spectroscopic characteristics of such edges and observe enhanced second-order nonlinearity originating from the strained zigzag edges. We also confirm that ultrasharp hexagonal nanoholes in MoS_2 grow along the most stable crystallographic directions despite potential stacking faults or instabilities in the crystal quality. Our results open the way to exploit a broad range of phenomena occurring at the edges of MoS_2 material, including the unique determination of crystal orientation for moiré engineering and strongly correlated phenomena in 2D material-based systems, as well as potential applications in TMD-based electrocatalysis and gas sensing.

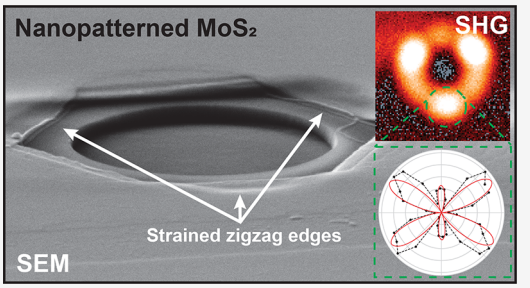

1. INTRODUCTION

An emerging family of transition metal dichalcogenides (TMDs) opened up avenues for diverse research and technological advancements. These materials combine two-dimensional (2D) physics with diverse chemical compositions, which in turn enable a number of advanced electronic, excitonic, and many-body phenomena, as well as possibilities for thickness- and stacking-dependent engineering of band gap and nonlinear optical properties.[1−6] Furthermore, the introduction of controllable stacking of individual TMD layers into heterostructures has emerged as a powerful method for constructing ultrathin multifunctional materials and devices.[1,7,8]

Structural defects strongly affect the physicochemical properties of TMDs and have paramount importance for their electronic applications, similar to the case of Si-based microelectronics.[9−12] It is worth noting that surface adatoms and adsorbed species, which are often disregarded in three-dimensional (3D) semiconductors, become increasingly important in TMDs because of their ultrathin and van der Waals nature.[13] Nonetheless, the edges, essentially one-dimensional (1D) or quasi-1D defects,[9] are the most distinct features of TMDs as they cause strong changes in the electronic structure,[14,15] leading to modified optical and magnetic responses, as well as chemical reactivity.[16−19]

The most Earth-abundant and widely studied TMDs are MoS_2 and WS_2. Their most stable polytypes are composed of S−metal−S layers with hexagonal symmetry dictating two principal edge configurations: zigzag (*zz*) and armchair (*ac*). At *zz* edges, MoS_2 and WS_2 exhibit several unique phenomena which are not observed in their continuous 2D or bulk 3D forms, namely, edge-localized metallic states,[20,21] ferromagnetism,[22,23] and enhanced electrocatalytic activity.[19] Numerous random edges can be generated by mechanical grinding of MoS_2 powders[24] or chemical synthesis of vertically aligned[25] or highly distorted[26] flakes. However, controllable fabrication of dense and precisely arranged *zz* edges in highly crystalline MoS_2 and WS_2 flakes without decreasing their lateral dimensions is a challenging nanofabrication task. State-of-the-art techniques typically imply two-step processing: (i) perforation of the disulfide flakes in the vertical direction and (ii) crystallography-guided in-plane etching to develop high-quality *zz* edges. The first step can be done using plasma/reactive ion etching through a lithography-defined mask,[27−29] focused ion beam patterning,[27] or laser ablation.[30] The second step comprises chemical wet-etching by H_2O_2-based[27] or potassium ferricyanide solution[28,29] or thermochemical etching in a controlled atmosphere.[30] When using SF_6 plasma etching, both steps can be combined (at the cost of somewhat reduced edge sharpness and spatial controllability).[31] Crystallography-driven in-plane chemical etching can also visualize the atomic orientation and relative angle of TMD flakes on a macro-

Received: June 6, 2023
Revised: July 17, 2023
Published: August 1, 2023

level.[27,30,31] Such techniques are of importance for the fabrication of emerging moiré superlattices,[32] a powerful platform to study new optical selection rules,[33] valley physics, and strongly correlated phenomena.[34,35] First-principles calculations of nanopore etching in MoS_2 are also gaining popularity nowadays.[36]

Strain strongly affects the electronic, optical, and other properties of MoS_2 flakes,[37−40] while a high breaking strain limit of >10% and Young's modulus of up to 250 GPa[41] facilitate MoS_2 incorporation into stretchable and strain-tuned optoelectronic devices. It was also shown that the native *zz* edges of mechanically exfoliated MoS_2 flakes introduce regions with alternating localized compressive and tensile strain, which in turn affect the excitonic properties.[42] However, no studies have been conducted on the impact of finely nanofabricated edges in MoS_2/WS_2 flakes on their optical properties. The mutual effects of the existing structural defects and nanofabricated edges in TMDs are poorly studied as well.

Here, we employ our recently reported nanofabrication technique[27] to produce etching pits bordered by ultrasharp *zz* edges in multilayer MoS_2 and WS_2. We performed a thorough microscopic characterization of the fabricated etching pits, which sheds light on the anisotropic wet etching of 2D disulfides. Careful evaluation of the edges and near-edge areas via Raman and second-harmonic-generation (SHG) spectroscopies revealed a complex interplay between the mechanical strain and optical nonlinearities introduced by the nanofabricated *zz* edges. The crystallographic and chemical differences affecting the anisotropic wet etching of MoS_2 vs WS_2 multilayers are addressed as well. We also demonstrate that the crystallography-guided wet etching highlights stacking faults and extended intergrown domains of other polytypes in MoS_2 flakes and, in this way, enables the vertical profiling of their quality.

2. METHODS

2.1. Sample Preparation and Nanofabrication. The nanofabrication steps were performed in Myfab Nanofabrication Laboratory, MC2 Chalmers. High-quality 2H-MoS_2 crystal (HQ graphene, The Netherlands) was used for exfoliation of tens of nanometers thick flakes by a Scotch tape technique. These flakes were transferred to polydimethylsiloxane (PDMS) stamps (Gel-Pak, USA) and then to n-doped 285 nm SiO_2/Si substrates (Graphene Supermarket, USA) by using the all-dry transfer method.[43] The zigzag edge-terminated hexagons were formed through a sequence of dry and wet etching processes, being able to choose their dimensions and density per unit area on the TMD flakes.[27] In brief, the substrates with MoS_2 flakes were covered with ARP 6200.13 resist (Allresist GmbH, Germany) to create a ∼550 nm thick e-beam patterned mask for dry etching of the circular holes in MoS_2. E-beam lithography was performed using the JEOL JBX 9300FS system (Japan) operating at 100 kV accelerating voltage. A dose of 450 $\mu C/cm^2$ was applied, and *n*-amyl acetate was used as a developer. Reactive ion etching of MoS_2 flakes through the ARP mask was performed using CHF_3 plasma in an Oxford Plasmalab 100 system (U.K.). CHF_3 gas flow was 50 sccm. Argon (40 sccm) was used as a carrier/supplementary gas. Radiofrequency generator forward power (RF power) was set to 50 W, and inductively coupled plasma (ICP) generator was not employed. The average vertical etching rate of MoS_2 by CHF_3 plasma was 10 nm/min. After CHF_3, a short (4 s) pulse of O_2 plasma (40 sccm of O_2, 40 W of RF power, 200 W of ICP power) was applied to remove the passivating fluorocarbon film from the etching pit walls. Then the remaining resist was removed, and wet etching of the flakes was performed at 65 °C in a 1:1:10 mixture of 31% H_2O_2, 25% NH_4OH, and deionized water. The optical characterization by Raman and SHG spectroscopies of the structures requires their minimum diameter to be ∼1−10 μm in order to be accessible with the smallest diffraction-limited spot size given by a high numerical aperture objective. Therefore, we chose 2−10 μm diameters of the dry-etched circular holes. For comparison, similar samples were fabricated based on WS_2 flakes.

2.2. Optical Characterization. *2.2.1. Raman Characterization.* Raman spectroscopy was performed at the Chalmers Materials Analysis Laboratory (CMAL). The measurements were carried out at room temperature with a commercially available setup (WITEC Alpha 300R) in a reflective geometry, with a 100× NA = 0.9 objective allowing for a diffraction-limited lateral resolution of ∼0.3 μm. A continuous wave excitation of 532 nm was set to a power of <0.5 mW to avoid sample heating while producing a strong enough Raman signal detected by the spectrometer, hosting an 1800 l/mm grating. The beam was scanned over the sample in a raster scan fashion to obtain a 5 × 5 μm^2 map. The spectra at each location were fitted to a Lorentzian function to track the position, intensity, and spectral width of the different Raman peaks present in the sample.

2.2.2. Second-Harmonic Generation Characterization. A home-built scanning nonlinear microscopy setup was used to perform SHG characterizations (see Figure S1). The strong optical field needed to induce nonlinear effects was achieved using pulsed laser excitation at λ = 1040 nm at a pulse repetition rate of 80 MHz and pulse duration of ∼100 fs, originating from a Ti:sapphire femtosecond laser (MaiTai HP Newport Spectra-Physics). The excitation energy (≈1.20 eV) is appropriate since it is far from the photoluminescence signal due to the MoS_2 excitonic features, around 1.90 eV.[44]

The 1040 nm excitation beam is sent first through a pair of linear polarizers that allow us to control both its power (on the order of 1 mW) and polarization direction, which we set to be horizontal, to reduce losses in the multiple reflections that take place along the setup. The polarized, collimated signal is then sent through another pair of optical elements consisting of a broadband linear polarizer and a half-wave plate so that the polarization direction on the sample can be controlled by rotating the $\lambda/2$ plate. The laser beam is further sent to fill the back aperture of a 40× air (NA = 0.95) objective, scanning over the sample with a piezostage in reflection geometry. The second-harmonic signal (at λ = 520 nm) is collected by the same objective and separated from the fundamental beam using a dichroic mirror and a short-pass filter to be finally focused into a 50 μm multimode fiber, connected to either a spectrometer (Andor 500i, Newton 920 CCD camera) or an avalanche photodiode (APD, IDQ, ID100 visible single photon detector). These configurations allow us to analyze the spectroscopic quality of the signal and perform SHG mapping, respectively.

2.3. Morphological Characterization. The morphology of the etching pits was analyzed by scanning electron microscopy (SEM) using an Ultra 55 microscope (Carl Zeiss, Germany). The images were taken at 1 and 5 kV accelerating voltage using the secondary electron detector. A tilted-view image was registered as well. SEM was performed at Chalmers Materials Analysis Laboratory (CMAL). Tapping-

https://doi.org/10.1021/acs.jpcc.3c03812
J. Phys. Chem. C 2023, 127, 15395−15405

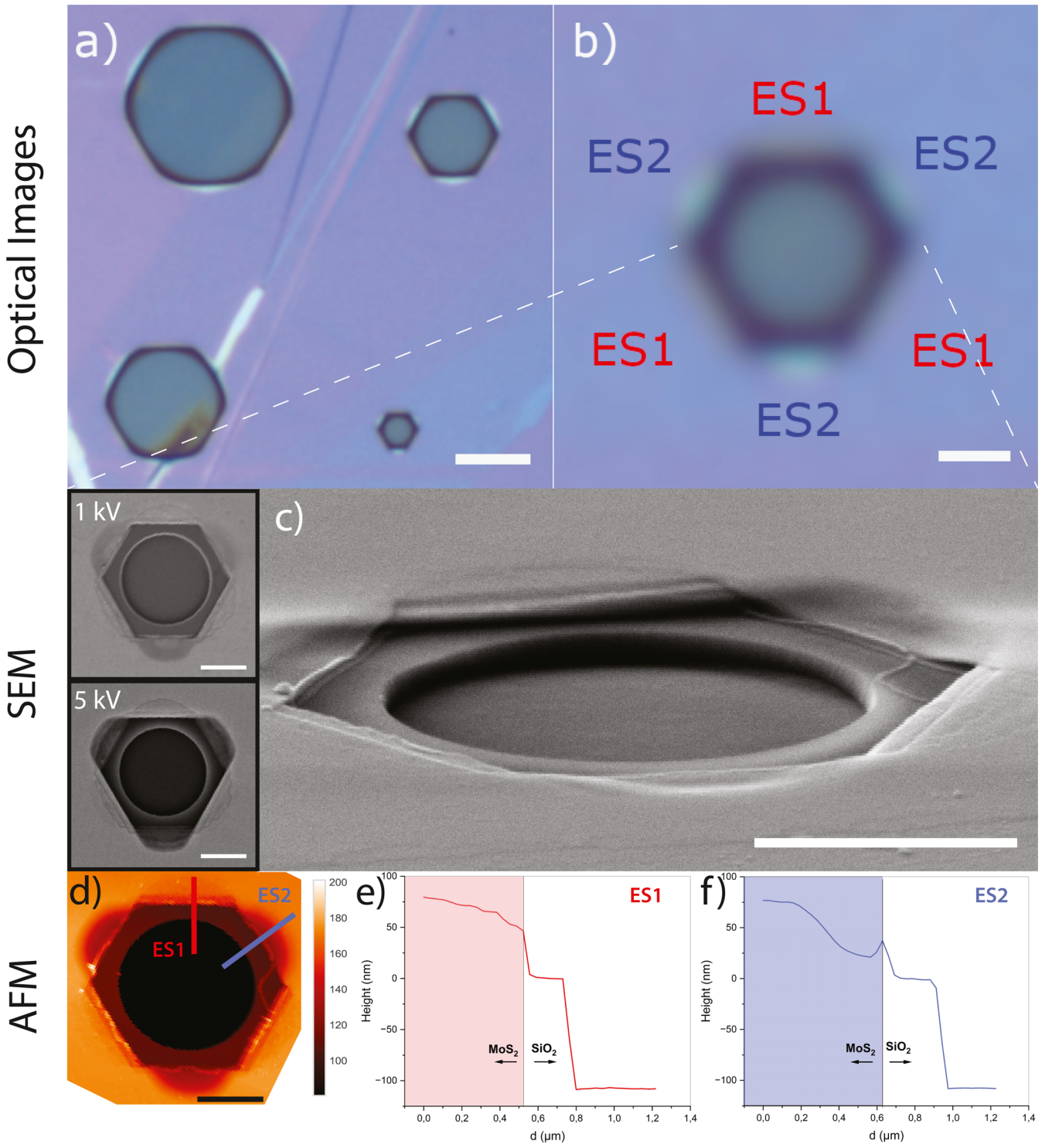

Figure 1. Hexagonal etching pits in MoS_2: (a) optical image of hexagons of different diameters (2, 5, 7, and 10 μm diameters) of initial holes etched in a ~75 nm thick MoS_2 multilayer (scale bar, 5 μm), (b) optical image of a 2 μm diameter hexagon, labeling the two edge sets (scale bar, 1 μm), (c) tilted/side SEM view of the same etching pit showing the sharp/straight and bent/strained sets of edges (scale bar, 1 μm); insets are top SEM views of 2 μm hexagon taken at a different accelerating voltage (top, −1 kV; bottom, −5 kV; scale bar, 1 μm), (d) AFM mapping, (e, f) cross sections of AFM scans showing the profile followed by the labeled lines in (d) for **ES1** (red) and **ES2** (blue).

mode atomic force microscopy (Bruker Dimension 3100 microscope) was used to assess the topography of the etched MoS_2. AFM was performed at Myfab Nanofabrication Laboratory, MC2 Chalmers. A custom Python code was used to extract and plot the relief profiles along certain lines perpendicular to the etching pit edges.

3. RESULTS AND DISCUSSION

3.1. Anisotropic Wet Etching of Multilayer MoS_2. The TMD nanopatterning technique used in this work combines a dry etching of lithography-defined circular holes and subsequent anisotropic wet etching governed by the crystal structure.[27] Figure 1a shows an optical image of hexagonal

https://doi.org/10.1021/acs.jpcc.3c03812
J. Phys. Chem. C 2023, 127, 15395−15405

etching pits formed from the initial circular holes of different diameters: 2, 5, 7, and 10 μm. In what follows, we use these diameter values to denote hexagons of different sizes, although the inscribed circle diameters of the final hexagons are always approximately 400 nm longer. Note that the hexagons etched in MoS_2 are significantly less sharp than the ones in WS_2 (Figure S2 and ref 27). An enlarged optical image of a 2 μm hexagon (Figure 1b) suggests a nonequivalency of two interlaced groups of its sides. SEM micrographs of the same hexagon taken at different e-beam accelerating voltages (Figure 1c) demonstrate the complex structure of this etching pit. The circular hole underneath the hexagon is a dry-etched pattern in the 285 nm thick SiO_2/Si substrate. It formed because the duration of the reactive ion etching (based on CHF_3 plasma) was chosen on purpose in such a way that the MoS_2 flake would be assuredly etched through. This replica also represents the diameter of an initial circular hole in MoS_2 before wet etching. When the SEM accelerating voltage is low (1 kV), the secondary electrons escape from the upper MoS_2 layers only, and an image resembling the optical micrograph is observed (Figure 1c, inset). The same appearance and topography of the hexagon and its edges can be found in the AFM images and the corresponding line scans (Figure 1d–f). Considering the top surface of the flake, we recognize two alternating edge sets (**ES**) bordering the hexagon: **ES1**, where the topmost layers are etched with stepped structures but the underlying layers are flat, and **ES2**, where the near-edge surface is smooth but bent downward (Figure 1b,c). SEM micrograph taken with higher (5 kV) accelerating voltage contains information from the underlying MoS_2 layers (Figure 1c, inset). The large cavities became visible underneath the bent superficial layers near **ES2**; they are followed again by the sharp edges formed by the subsequent layers in a downward direction. A similar profile can be elucidated when comparing 1 kV and 5 kV SEM micrographs of 5 μm hexagon (Figure S3). This bending of upper layers near **ES2** and the flat layers flooring the cavities (with the same size of the hexagonal hole as the upper layers) is also seen clearly in a side view SEM of a 2 μm etching pit (Figure 1c).

The shape of the etching pits and the differences between **ES1** and **ES2** provide crucial information about the crystallography-guided etching mechanism. S–Mo–S layers with trigonal prismatic coordination of molybdenum (e.g., most stable 2H polytype) have hexagonal symmetry, which predetermines the two key edge structures: armchair (*ac*) and zigzag (*zz*). The latter includes molybdenum-zigzag (Mo-*zz*) and sulfur-zigzag (S-*zz*) edge structures. The corresponding *ac* and *zz* directions in the crystal alternate with a 30° step. Mechanically exfoliated MoS_2 flakes can have macroscopic edges not parallel to these directions, but their atomic structures can be described as a mix of *ac* and *zz* edges in varying percentages.

In our two-step process, the mask-mediated dry etching forms precisely positioned circular holes. Their borders can be considered as an ultimately random combination of *ac* and *zz* edges. It is a unique feature of our CHF_3-based etching recipe that it enables vertical etching throughout MoS_2 basal planes but passivates both *ac* and *zz* edges equally well. Dry etching based on CHF_3 plasma stands out from other carbon-free plasmas (e.g., O_2 plasma, SF_6 plasma, etc. due to the possibility of the formation of an inhibiting fluorocarbon film on the sample surface. At certain recipe parameters (e.g., gas flow, RF power, supplementary gases content, etc.), this layer efficiently passivates the walls of the etching pits but still allows vertical etching of the materials.[45,46] CHF_3-based etching used here produces arbitrary patterns in MoS_2 flakes (including circular holes) with a minimal undercut. Hence it is more versatile compared to SF_6-based plasma, which inevitably combines vertical and anisotropic in-plane etching of TMDs.[31] In our case, anisotropic wet etching is a separate second step. In this process, the dry-etched circular holes act as large penetrating defects propagating throughout the entire MoS_2 flake and enable a simultaneous in-plane etching of all the layers by an H_2O_2-based solution. We briefly discuss the chemical aspects of the wet etching in Supporting Information, section S3.

Let us consider an etching pit that appears at an arbitrary point of the S–Mo–S slab. With respect to its center, there are six in-plane directions orthogonal to *ac* edges (⊥-*ac*) and another six directions orthogonal to *zz* edges (⊥-*zz*). The latter becomes differentiated into two sets alternating with a 60° step: ⊥-Mo-*zz* and ⊥-S-*zz* (Figure 2a). The arrangement

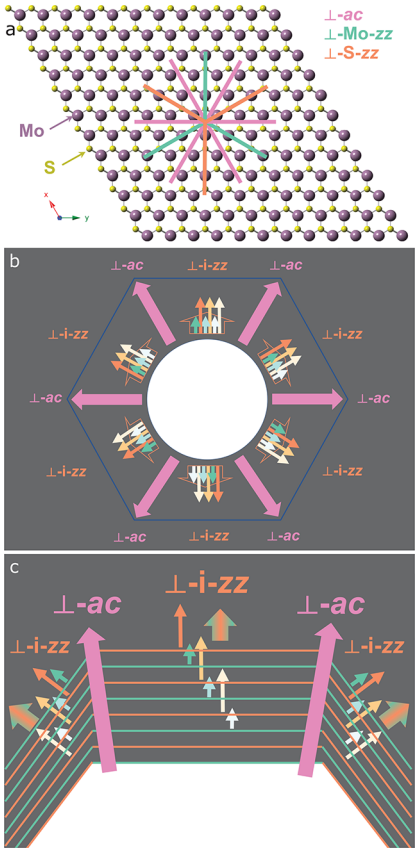

Figure 2. (a) Schematic for ⊥-*ac*, ⊥-Mo-*zz*, and ⊥-S-*zz* directions in monolayer MoS_2. (b, c) Structure of the etching pit walls in ideal 2H-MoS_2 far enough from the flake surface: faster-etched zigzag edges (red) are sandwiched between the slower-etched zigzag edges (green). All the walls are structurally equivalent, with a one-layer shift up or down. Due to the mutual influence of the adjacent layers, all six i-*zz* crystal faces are etched at the same rate.

of ⊥-*ac*, ⊥-Mo-*zz*, and ⊥-S-*zz* directions predetermines hexagonal or triangular symmetry of anisotropic etching pits in MoS_2 (and similar structures) depending on the stability of *ac*, Mo-*zz*, and S-*zz* edges.

To explain the formation of observed etching pits (Figure 1), we will start by considering an individual layer etching and then discuss the case of the multilayer structure. Intuitively, the

https://doi.org/10.1021/acs.jpcc.3c03812
J. Phys. Chem. C 2023, 127, 15395–15405

in-plane etching of an initial hole in a disulfide layer can be seen as an inverted analog of MoS_2 monolayer growth (e.g., by chemical vapor deposition, CVD[47]) and follow the same crystallographic considerations, including Wulff constructions.[48] The shape of the etching pit is going to be determined by the etching rate of different crystal faces. In an individual disulfide layer, the free energy of the edges should be considered instead. The slow-etching edges become the largest, and the fast-etched ones either become smaller or eventually disappear. The edge energies are affected by the chemical potentials of Mo and S in a particular environment. In the case of chemical wet etching, they will be strongly altered by composition, concentration (including its evolution with time), and temperature of the etching liquid. Mo-*zz* and S-*zz* edges are more stable compared to *ac* edges in a wide range of other constructive and destructive conditions, e.g., CVD growth[47] and chemical/physicochemical etching,[27−29,31,49] respectively. The exact energy difference between Mo-*zz* and S-*zz* determines the final shape and termination of the pits. In turn, the energy difference between the *ac* and the least stable *zz* edge will define the etching time required to achieve a well-developed pit and its sharpness. Usually, a substantial stability difference between Mo-*zz* and S-*zz* results in triangular pits upon long-enough etching of MoS_2 monolayer.[29] This is also true for the H_2O_2-based wet etching used in this work, as demonstrated previously using WS_2 monolayer.[27] However, if the chemical environment dictates equal stability of Mo-*zz* and S-*zz*, hexagonal etching pits are formed in MoS_2 monolayer.[30] In Supporting Information, section S4, we briefly review the reports on the structure/termination of MoS_2 *zz* edges at different etching conditions and their effect on the etching pit shape.[27,29,30,50−52] However, direct identification of the most stable *zz* configuration upon H_2O_2-based wet etching is beyond the scope of this article.

In this work, we used multilayer 2H-MoS_2 as a parent crystal; i.e., antiparallel A_1B_2 stacking of adjacent layers is expected in the exfoliated ∼75 nm thick flakes. Hence, on the border of the etching pit, the Mo-*zz* edges of one layer are located above the S-*zz* of the next layer and *vice versa*. Although the interlayer van der Waals bonds might be insufficient to limit the chemical reactivity of adjacent S−Mo−S slabs, the steric limitations for mass transport of oxidative agents and reaction products will result in a significant impact of one neighboring layer on another. Regardless of the relative stability of Mo-*zz* and S-*zz* in the chosen wet etching conditions, faster-etched *zz* edges of one layer are going to be sandwiched between the slower-etched *zz* edges directions of the very next upper/lower layers, and *vice versa* (Figure 2b,c). Conversely, the fastest-etched *ac* edges coincide in all the layers. Compared to the independent layer, the etching of more (less) reactive zigzag edges is decelerated (accelerated) due to the slower (faster) etching of two neighboring layers. Eventually, a stack of "interlaced zigzag" (i-*zz*) edges with a unified etching rate is formed. In other words, the further etching propagates along six slower-etched equivalent ⊥i-*zz* directions and six faster-etched ⊥-*ac* directions (Figure 2b,c). As a result, even upon different Mo-*zz* and S-*zz* stabilities under given etching conditions, hexagonal etching pits can be formed. This is a drastic difference of multilayer 2H-MoS_2 from the 1H-MoS_2 monolayer, where no i-*zz* can be formed, and triangular etching pits should develop in the case of different Mo-*zz* and S-*zz* stability. We also briefly discuss the difference between 2H-Mo_2 and 2H-WS_2 upon crystallography-guided wet etching in Supporting Information, section S5.

The flake's surface/topmost layer is an obvious disruptor of the i-*zz*. The top layer of the flake is the least affected by any interlayer interactions. Therefore, it strives to form a triangular hole. This tendency is clearly seen in Figure 1c upon a closer look at **ES1** and is discussed in more detail in Supporting Information, section S6.

We assume the cavities under the **ES2** regions (Figure 1c, inset, Figure S2b) are formed due to relatively large intergrown polytype domain(s) in the flake studied here. The guest MoS_2 polytypes in the host 2H-MoS_2 phase usually contain several consecutive S−Mo−S layers with parallel orientation.[53] Being randomly distributed along the vertical direction of the flake, the polytype intergrowths uniformly propagate for large distances in the lateral direction of MoS_2 multilayer and, in this way, usually are the same across the entire 50−100 μm flakes used in this work. This is corroborated by a similar etching profile of the neighboring 2 μm (Figure 1c) and 5 μm (Figure S3) hexagons. An additional discussion of stacking faults and polytype intergrowths in MoS_2 is given in Supporting Information, section S7.[49,53,54] When several subsequent S−Mo−S layers are oriented parallel to each other, their less stable zigzag directions are congruent, and at least a few nanometers deep part of the crystal is etched in a triangle-like shape. Similarly, a high local concentration of the stacking faults can also destabilize i-*zz* faces and promote triangular etching. At a certain distance from the polytype intergrowth (or a cluster of stacking faults), the i-*zz* structure equilibrates again, and a "normal" hexagon etching pit continues (see the bottom part of the flake on Figure 1c and Figure S2b). The parent 2H-MoS_2 flake used in our experiments seems to contain a quite extended intergrown domain with a parallel orientation of the S−Mo−S layers. Interestingly, it is rotated 60° with respect to the topmost part of the flake. In turn, individual stacking faults affect just a few neighboring layers. Therefore, they seem responsible for minor distortions like the goffered structure on the bottom layers at the **ES2** side visible well in the 5 μm hexagon (Figure S5).

In general, stacking faults and, especially, sizable domains of intergrown guest polytypes indicate that the original crystal is of insufficient quality. However, in our situation, the triangle-like cavities caused by a polytype intergrowth have led to a notable downward bending of the upper MoS_2 layers as they lack material beneath (Figure 1c). The large size of the unsupported region compared to the lattice constant and the considerable flexibility of MoS_2 do not allow the crystal enough rigidity to stay suspended. Thus, it bends down until it meets the intact layers at the bottom of the cavities and causes strained regions (Figure 1c,d). This unusual feature allowed us to study the local stress and corresponding spectroscopic response in the bent (strained) near-zigzag-edge area of MoS_2.

3.2. Raman Characterization of the Edge Region.

Raman spectroscopy is a powerful tool that allows studying of vibrational fingerprints and related physical properties of various materials noninvasively. Multilayer TMDs in their 2H phase exhibit two Raman peaks corresponding to the in-plane (E_{2g}) and out-of-plane (A_{1g}) vibrations.[55] These modes can experience a peak shift and intensity change due to strain, thickness, or doping effects,[38,56,57] which may allow the identification of specific features or regions within a spatially resolved Raman intensity map.

https://doi.org/10.1021/acs.jpcc.3c03812
J. Phys. Chem. C 2023, 127, 15395−15405

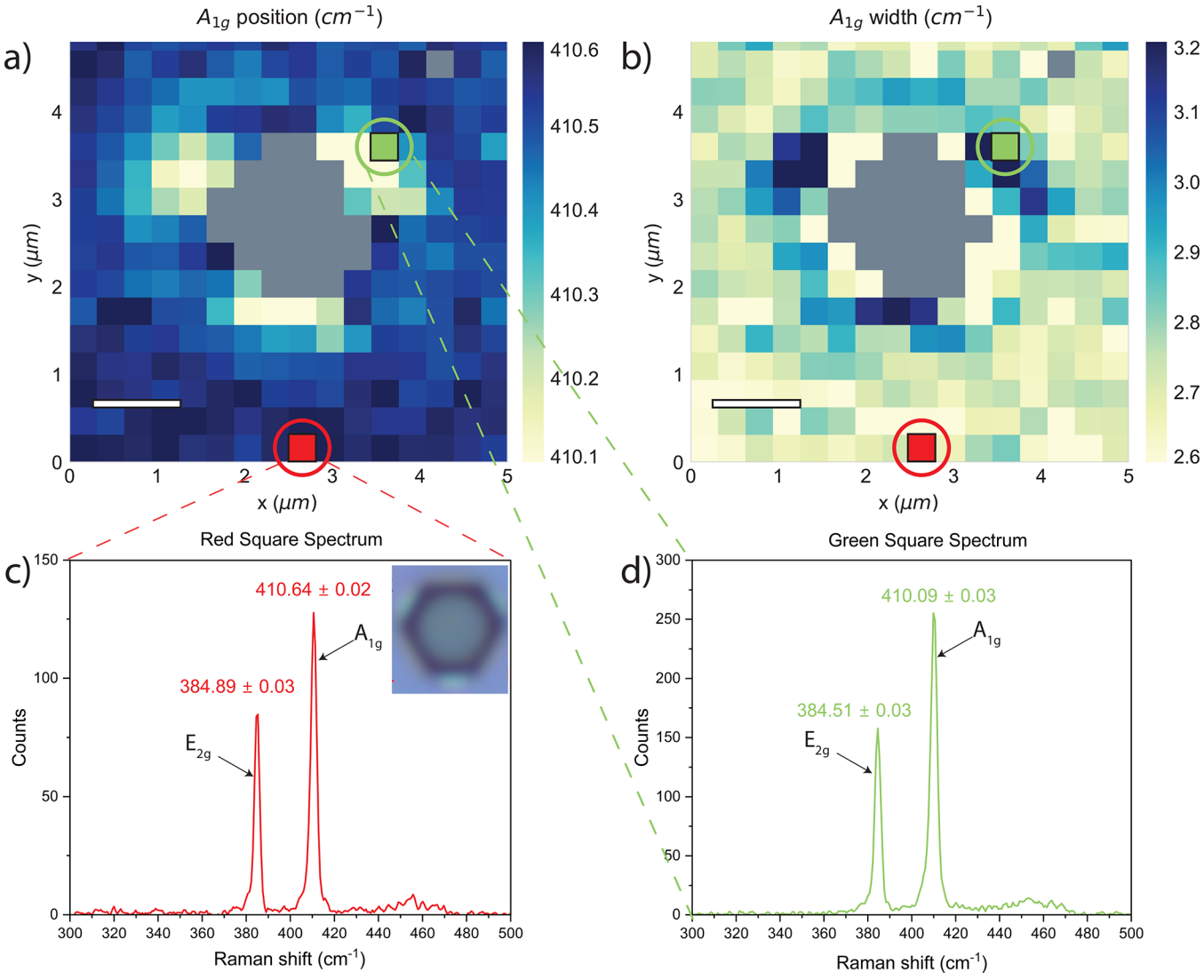

Figure 3. Raman maps of 2 μm hexagon in MoS_2 showing the spectral position (a) and fwhm (b) of out-of-plane vibrational mode A_{1g}. The scale bar is 1 μm. The etched region and edges are recognizable with the high-NA objective diffraction-limited spot (~0.3 μm). Selected spectra at the **ES2** region (c, green) and the region far from the defects (d, red) are displayed. The inset in (c) shows the optical image of the 2 μm hexagon, which correlates well with the Raman maps in (a) and (b).

Here, we use Raman spectroscopy to identify the strained regions caused by the extended cavities formed upon wet etching of the polytype intergrowth/stacking faults hidden in the middle of the flake's thickness (see section 3.1 and Figure 1c). Raman maps corresponding to the out-of-plane mode (A_{1g} ~ 410 cm^{-1}) on the 2 μm hexagon show a 0.55 cm^{-1} redshift at the edges of **ES2** (Figure 3a), together with a 20% increase of the full width at half-maximum (fwhm) (Figure 3b). The signal change is highly localized at the strained regions, while the material around the sharp edges of **ES1** does not show a significant variation with respect to the bulk away from the hexagon. As discussed above, the **ES2** hosts strained edges due to the lack of supporting material below the topmost MoS_2 layers. Moreover, the increase in the peak width suggests the presence of different phonon contributions within the laser excitation volume interacting with the material at those locations, which results in different peaks shifting with respect to the original A_{1g} mode. These are possibly due to highly localized strain and variations in the thickness of the material, which are not resolved by the spectrometer and therefore appear as the Raman peak width. The absence of any electrical contacts on the flake and the minimal signal change at the **ES1** set of edges rule out the possibility of a shift caused by sample charging. A similar behavior is observed in the E_{2g} mode (compare Figure 3c and Figure 3d; also see Supporting Information, Figure S6). It confirms that the strained **ES2** suffers from a nonuniform strain in both the in-plane and the out-of-plane directions.

All these observations support the impact of the strain on the Raman spectra of MoS_2, which was also observed in the studies by Zhu et al.[58,59] In those studies, the strain was systematically engineered, revealing its impact on the Raman and photoluminescence properties. Similar to our findings, a redshift of the A_{1g} mode was observed upon increasing the tensile strain. Furthermore, several works have reported that compression and tension have an impact on the Raman modes of MoS_2 and opposite Raman shifts, redshift and blueshift, were observed for tension and compression, respectively.[60−63] Li et al. studied the Raman modes shifts caused by nonuniform biaxial strain in MoS_2 monolayers transferred onto an array of

https://doi.org/10.1021/acs.jpcc.3c03812
J. Phys. Chem. C 2023, 127, 15395−15405

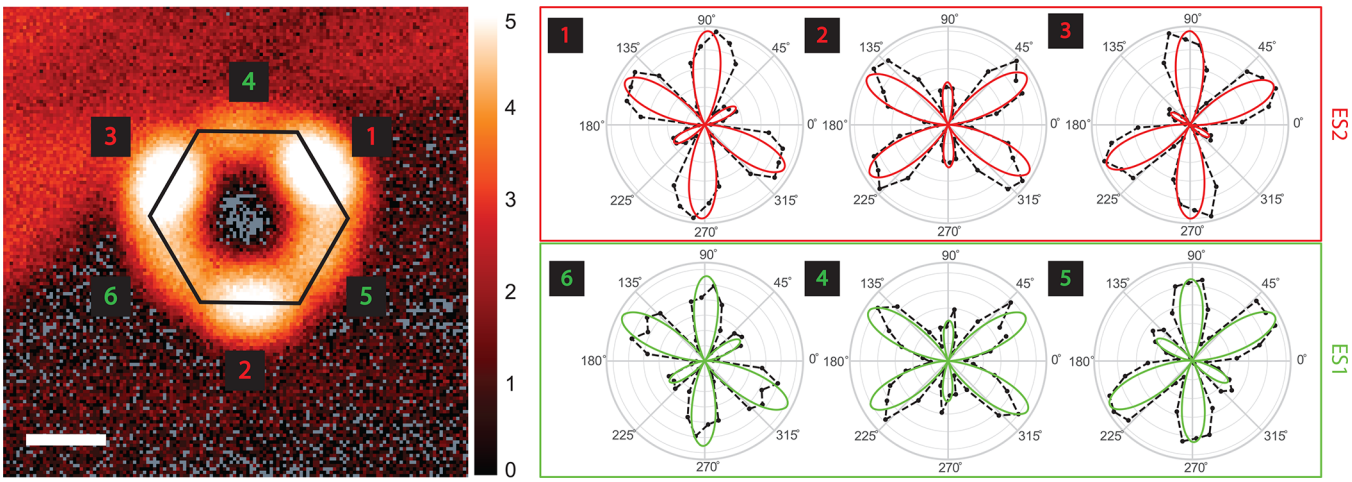

Figure 4. Second harmonic generation measurements: left plot shows a scan of the 2 μm hexagon demonstrating an increased intensity at **ES1** (green labels) and especially at strained **ES2** (red labels) edges. The intensity is color-coded in a logarithmic scale. The scale bar is 1 μm. Polar plots on the right show polarization-dependent measurements with the intensity dependence versus an angle at all the edges, together with the fitting to eq 1.

SiO_2 nanocones.[64] The strained MoS_2 exhibited redshift of both E_{2g} and A_{1g} modes. At the apex of the nanocone, MoS_2 exhibited the highest level of strain, whereas it was lower between the nanocones. A similar nonuniform stress can be expected at the **ES2** in our work, with the most strained regions near the hexagon vertices and much less strained MoS_2 in the middle of the corresponding edges (Figure 1c). Based on the calculated Raman spectra, Li et al. estimated ~0.57% biaxial tensile strain (averaged across the 450 nm diameter laser spot) for a 0.6 cm^{-1} redshift of A_{1g},[64] which is close to the 0.55 cm^{-1} redshift observed in our work here. For the calculations of theoretical biaxial-strain-dependent Raman spectra, Li et al. employed the first-principles density-functional perturbation theory implemented in the QUANTUM-ESPRESSO package.[64] The calculations were further correlated with experimental Raman spectra and the strain values measured by scanning tunneling microscopy.[64]

Our etched structures can concentrate the strain into micrometer-sized areas defined by the size of the etching pit. AFM of one of the **ES1** edges (Figure 1e) shows a height variation of ~66% of the initial flake height, suggesting a pronounced symmetry breaking of the crystal structure compared to the **ES2**, which has a step-like profile (Figure 1f). It is of interest to investigate the contribution of symmetry breaking and strain generated at the edges of **ES1** to the enhancement of second-order nonlinearities, as demonstrated in the following analysis.

3.3. Second-Harmonic Generation from the Edge Region. Nonlinear optical processes taking place in crystals give access to important material properties and have been studied since the short-pulsed lasers enabled widespread access to intense electric fields. Second-harmonic generation (SHG) is an important technique used to study the crystallographic properties of materials, with special importance for the characterization of TMDs. This is in part due to the strong polarization dependence of the second-harmonic signal, which finds a very direct application in the nanofabrication of angle-aligned heterostructures and moiré superlattices.[32,65] The polarization dependence of the signal stems from the nonlinear nature of the effect, the frequency of which is 2 times the one of the pump laser.

The setup described in the Methods section above is suitable for measuring the intensity component parallel to the incoming laser excitation in polarization-dependent SHG measurements. This is possible since the rotation of the polarization plane of the field hitting the sample can be rotated by the $\lambda/2$ plate, while the polarization of the SHG signal is rotated back by the same angle when the signal passes through the same waveplate in the detection channel. Thus, the polarizer will always recover the intensity component of the field coming from the sample that is parallel to the original excitation.

SHG mapping performed on the patterned flake (Figure 4, left) allows for the recognition of areas of different thicknesses caused by mechanical exfoliation and strained defects, as well as the flake edges and etched hexagons. Notable SHG signal from unpatterned areas is observed, suggesting the presence of crystal defects or stacking faults that make the crystal structure deviate from the ideal 2H-MoS_2 phase, which should not exhibit any SHG due to its inversion-symmetric structure.[66] Remarkably, we observe a signal increase of up to 1−2 orders of magnitude at the **ES1** of the 2 μm hexagon and up to 5 orders of magnitude increase at the strained edges of **ES2** (Figure 4, left). The SHG signal is larger when the asymmetry of the crystal structure increases; thus, an intensity increase at the edges compared to the bulk material is expected,[18] as well as an increase at the edges forming **ES2** due to additional symmetry break caused by strain, ($I_{bulk} < I_{ES1} < I_{ES2}$). Our results experimentally confirm these expectations and also provide quantitative measures of the SHG enhancement caused by the symmetry break at the edges and by strain.

Edge state modulation of the electronic band structure may result in a bandgap reduction at the edge of the crystal.[67] Studies performed on CVD-grown MoS_2 domains showed an increase of the second-harmonic signal due to a resonance of the incoming excitation with the bandgap present at the edge, which allowed the identification of different types of edges. However, the excitation used in our experiments (1040 nm) is far from the reported resonance wavelength reported for zigzag edges, ruling out this possibility.[68] Furthermore, the wavelength of our excitation excludes signal enhancement due to resonances with both intralayer and interlayer excitons present in MoS_2.[69]

https://doi.org/10.1021/acs.jpcc.3c03812
J. Phys. Chem. C 2023, 127, 15395−15405

To verify the quality and nature of wet-etched MoS_2 edges, we performed polarization-resolved SHG measurements (Figure 4, panels 1−6). Our results show one-to-one correspondence in the polarization-resolved SHG profiles (and therefore in crystal symmetry) between edges produced on the opposite sides of the hexagon. One of these edges is bent, and the other one is sharp. For example, edges 1 and 6 exhibit the same SHG angular profile but different overall intensity of the signal (Figure 4). The latter is due to additional enhancement by strain at the **ES2** edges. The polarization-resolved SHG data can be described by the following equations (see Supporting Information, section S9):

$$I(\theta) = |P_{2\omega}(\theta)|^2 \tag{1}$$

$$P_{2\omega}(\theta) = \chi^{(2)}_{xxx} \cos^3\theta + 3\chi^{(2)}_{xxy} \cos^2\theta \sin\theta + 3\chi^{(2)}_{xyy} \sin^2\theta \cos\theta + \chi^{(2)}_{yyy} \sin^3\theta \tag{2}$$

Here, angle $\theta = \theta' - \phi$ includes both the angle between the laser polarization with respect to the MoS_2 crystal structure (θ') and with respect to the laboratory frame (ϕ), respectively. The fitting allows extraction of the relative strength of the elements of the $\chi^{(2)}$ tensor, characterizing the second-harmonic response of our structures (Table 1). The polarization-resolved

Table 1. Fitted Parameters for the $\chi^{(2)}$ Tensor Extracted from SHG Measurements[a]

ES2	edge 1	edge 2	edge 3
$\chi^{(2)}_{xxx}$	0.50 ± 0.08	1.00 ± 0.04	1.00 ± 0.05
$\chi^{(2)}_{xxy}$	−0.25 ± 0.05	−0.30 ± 0.05	0.00 ± 0.08
$\chi^{(2)}_{xyy}$	−0.97 ± 0.03	−0.76 ± 0.05	−0.86 ± 0.06
$\chi^{(2)}_{yyy}$	0.28 ± 0.06	−0.20 ± 0.04	0.15 ± 0.06
ES1	edge 6	edge 4	edge 5
$\chi^{(2)}_{xxx}$	0.69 ± 0.08	1.00 ± 0.04	0.99 ± 0.05
$\chi^{(2)}_{xxy}$	−0.14 ± 0.06	−0.25 ± 0.05	−0.12 ± 0.05
$\chi^{(2)}_{xyy}$	−1.00 ± 0.04	−0.87 ± 0.04	−0.85 ± 0.04
$\chi^{(2)}_{yyy}$	0.20 ± 0.07	0.01 ± 0.07	0.38 ± 0.06

[a]The edge numbers and their order in the table correspond to Figure. 4.

patterns exhibit the 6-fold-like pattern (Figure 4), which is characteristic of TMD crystal structure,[70] with a larger intensity in the direction parallel to the armchair edges[71] (hence, perpendicular to the zigzag edges). Remarkably, our polarization-resolved data reveal significant deviations from the ideal 6-fold patterns. Specifically, we observe that the arm perpendicular to the edge exhibits weaker intensity compared to the two arms along the other two armchair directions. This discrepancy can be attributed to the reduced symmetry at the edge, allowing us to determine the edge direction exclusively through polarization-resolved SHG measurements and confirming their zigzag nature. The polarization-resolved fits clearly demonstrate that the edges produced on the opposite sides of the hexagon are described by comparable $\chi^{(2)}$ tensor components, highlighting their qualitative similarity. Furthermore, our results show that the strained **ES2** edges still preserve a high-quality crystal orientation in accordance with their polarization-resolved SHG patterns, and thus, the etching of the layers is highly confined in the direction parallel to the plane of the sample without invading adjacent layers in the vertical direction.

Results of our work confirm that three of the hexagon edges provide a high-quality platform to study one-dimensional, edge-related physical processes while the other three may provide a platform for studies of strained and suspended TMD for structures smaller than <1 μm. The edge orientation is respected along the zigzag directions of the crystal, as was the case for hexagons on WS_2,[27] making anisotropic wet etching a solid method to uniquely determine the lattice orientation of TMD crystals. Moreover, the peculiarities of the etching pit morphology allow vertical profiling of the stacking faults density and quality of the MoS_2 flakes, while the second-harmonic signal from unpatterned areas may highlight the deviations from the ideal 2H crystal phase. It would enable the differentiation of parallel and antiparallel stacking upon fabrication of angle-aligned heterostructures and the additional modality to study different moiré patterns even without using an SHG setup.

4. CONCLUSIONS

In summary, we demonstrated crystallography-driven anisotropic etching of MoS_2 multilayers and thoroughly correlated the morphological features of the etching pits (revealed by SEM and AFM) with Raman and SHG signals sensitive to local crystal defects and mechanical stress. We explained the propagation of the oxidative wet etching along MoS_2 crystal directions considering the relative stability of *zz* and *ac* edges, the interaction between adjacent S−Mo−S layers, and the role of stacking faults and polytype intergrowths. Similarities and dissimilarities with WS_2 etching[27] (especially the different relative stability of *ac* and *zz* edges) are systematically addressed as well. Typically, 2H-MoS_2 stacking results in hexagonal etching pits with walls composed of interlaced atomically sharp Mo-*zz* and S-*zz* edges. However, the hexagonal pits studied here had additional cavities with triangular symmetry, which were associated with a polytype intergrowth hidden in the middle of the flake and containing S−Mo−S layers with parallel orientation. These cavities caused the bending of the upper MoS_2 layers, which resulted in a distinct stress-related shift on the room-temperature Raman features and up to 5 orders of magnitude enhancement of SHG signal compared to the unpatterned MoS_2 areas.

This study extends our understanding of the zigzag edge enriched features fabricated using lithography-assisted dry etching and oxidative anisotropic wet etching of MoS_2 multilayers compared to other TMDs. It also highlights the applicability of anisotropic wet etching as a platform for the study of one-dimensional physics in TMD crystals near the high-quality and well-oriented edges of the etching pits, together with a unique and accessible way of determining the orientation of the crystal. This may find applications in producing moiré heterostructures and studying highly correlated phenomena in 2D material-based systems.[32,72,73] The understanding of the mechanisms for the enrichment of TMD crystals with zigzag edges is also important for the development of next-generation nanopatterned catalysts, stretchable gas-sensing films, and metamaterials for all-TMD nanophotonics.[74,75]

■ ASSOCIATED CONTENT

Supporting Information

The Supporting Information is available free of charge at https://pubs.acs.org/doi/10.1021/acs.jpcc.3c03812.

https://doi.org/10.1021/acs.jpcc.3c03812
J. Phys. Chem. C 2023, 127, 15395−15405

(Section S1) Second harmonic generation setup; (section S2) additional optical and SEM images of the samples; (section S3) additional discussion on chemical aspects of H_2O_2-based wet etching; (section S4) literature about MoS_2 *zz* edge termination at different etching conditions; (section S5) the difference between 2H-MoS_2 and 2H-WS_2 upon crystallography-guided wet etching; (section S6) effect of topmost MoS_2 layer on the i-*zz* structure; (section S7) stacking faults and intergrown polytype domains in 2H-MoS_2; (section S8) additional Raman spectroscopy maps of 2 μm hexagon; (section S9) SHG intensity derivation (PDF)

AUTHOR INFORMATION

Corresponding Author

Timur O. Shegai − *Department of Physics, Chalmers University of Technology, 412 96 Göteborg, Sweden;* orcid.org/0000-0002-4266-3721; Email: timurs@chalmers.se

Authors

Adrián Dewambrechies − *Department of Physics, Chalmers University of Technology, 412 96 Göteborg, Sweden;* Present Address: Department of Physics, Freie Universität Berlin, 14195 Berlin, Germany

Alexander Yu. Polyakov − *Department of Physics, Chalmers University of Technology, 412 96 Göteborg, Sweden; SMENA Catalysis AB, 412 96 Göteborg, Sweden;* orcid.org/0000-0002-3781-1881

Betül Küçüköz − *Department of Physics, Chalmers University of Technology, 412 96 Göteborg, Sweden*

Complete contact information is available at: https://pubs.acs.org/10.1021/acs.jpcc.3c03812

Author Contributions

[‖]A.D. and A.Yu.P. contributed equally.

Notes

The authors declare no competing financial interest.

ACKNOWLEDGMENTS

The authors acknowledge funding from the Swedish Research Council (VR Miljö Project, Grant 2016-06059, and VR Project, Grant 2017-04545), the Knut and Alice Wallenberg Foundation (Grant 2019.0140), Chalmers Area of Advance Nano, 2D-TECH VINNOVA Competence Center (Grant 2019-00068), and Olle Engkvist foundation (Grant 211-0063). This work was performed in part at Myfab Chalmers and at the Chalmers Material Analysis Laboratory, CMAL.

REFERENCES

(1) Novoselov, K. S.; Mishchenko, A.; Carvalho, A.; Neto, A. H. C. 2D materials and van der Waals heterostructures. *Science* **2016**, *353*, aac9439.

(2) Guo, H.; Lu, N.; Wang, L.; Wu, X.; Zeng, X. C. Tuning Electronic and Magnetic Properties of Early Transition-Metal Dichalcogenides via Tensile Strain. *J. Phys. Chem. C* **2014**, *118*, 7242−7249.

(3) Xu, X.; Trovatello, C.; Mooshammer, F.; Shao, Y.; Zhang, S.; Yao, K.; Basov, D. N.; Cerullo, G.; Schuck, P. J. Towards compact phase-matched and waveguided nonlinear optics in atomically layered semiconductors. *Nat. Photonics* **2022**, *16*, 698−706.

(4) Manzeli, S.; Ovchinnikov, D.; Pasquier, D.; Yazyev, O. V.; Kis, A. 2D transition metal dichalcogenides. *Nat. Rev. Mater.* **2017**, *2*, 17033.

(5) Mak, K. F.; Lee, C.; Hone, J.; Shan, J.; Heinz, T. F. Atomically Thin MoS_2: A New Direct-Gap Semiconductor. *Phys. Rev. Lett.* **2010**, *105*, 136805.

(6) Zhu, J.; Hu, L.; Zhao, P.; Lee, L. Y. S.; Wong, K.-Y. Recent Advances in Electrocatalytic Hydrogen Evolution Using Nanoparticles. *Chem. Rev.* **2020**, *120*, 851−918.

(7) Jin, C.; Ma, E. Y.; Karni, O.; Regan, E. C.; Wang, F.; Heinz, T. F. Ultrafast dynamics in van der Waals heterostructures. *Nat. Nanotechnol.* **2018**, *13*, 994−1003.

(8) Cai, Y.; Xu, K.; Zhu, W. Synthesis of transition metal dichalcogenides and their heterostructures. *Mater. Res. Express* **2018**, *5*, 095904.

(9) Lin, Z.; Carvalho, B. R.; Kahn, E.; Lv, R.; Rao, R.; Terrones, H.; Pimenta, M. A.; Terrones, M. Defect engineering of two-dimensional transition metal dichalcogenides. *2D Mater.* **2016**, *3*, 022002.

(10) Liang, Q.; Zhang, Q.; Zhao, X.; Liu, M.; Wee, A. T. S. Defect Engineering of Two-Dimensional Transition-Metal Dichalcogenides: Applications, Challenges, and Opportunities. *ACS Nano* **2021**, *15*, 2165−2181.

(11) Addou, R.; Colombo, L. In *Defects in Two-Dimensional Materials*; Addou, R., Colombo, L., Eds.; Elsevier, 2022; pp 1−5.

(12) McDonnell, S.; Reinke, P. In *Defects in Two-Dimensional Materials*; Addou, R., Colombo, L., Eds.; Elsevier, 2022; pp 89−117.

(13) Komsa, H.-P.; Krasheninnikov, A. V. In *Defects in Two-Dimensional Materials*; Addou, R., Colombo, L., Eds.; Elsevier, 2022; pp 7−41.

(14) Krishnamurthi, S.; Farmanbar, M.; Brocks, G. One-dimensional electronic instabilities at the edges of MoS_2. *Phys. Rev. B* **2020**, *102*, 165142.

(15) Davelou, D.; Kopidakis, G.; Kaxiras, E.; Remediakis, I. N. Nanoribbon edges of transition-metal dichalcogenides: Stability and electronic properties. *Phys. Rev. B* **2017**, *96*, 165436.

(16) Lin, K.-I.; Ho, Y.-H.; Liu, S.-B.; Ciou, J.-J.; Huang, B.-T.; Chen, C.; Chang, H.-C.; Tu, C.-L.; Chen, C.-H. Atom-Dependent Edge-Enhanced Second-Harmonic Generation on MoS_2 Monolayers. *Nano Lett.* **2018**, *18*, 793−797.

(17) Xiao, S.-L.; Yu, W.-Z.; Gao, S.-P. Edge preference and band gap characters of MoS_2 and WS_2 nanoribbons. *Surf. Sci.* **2016**, *653*, 107−112.

(18) Yin, X.; Ye, Z.; Chenet, D. A.; Ye, Y.; O'Brien, K.; Hone, J. C.; Zhang, X. Edge Nonlinear Optics on a MoS_2 Atomic Monolayer. *Science* **2014**, *344*, 488−490.

(19) Jaramillo, T. F.; Jørgensen, K. P.; Bonde, J.; Nielsen, J. H.; Horch, S.; Chorkendorff, I. Identification of Active Edge Sites for Electrochemical H_2 Evolution from MoS_2 Nanocatalysts. *Science* **2007**, *317*, 100−102.

(20) Bollinger, M. V.; Lauritsen, J. V.; Jacobsen, K. W.; Nørskov, J. K.; Helveg, S.; Besenbacher, F. One-Dimensional Metallic Edge States in MoS_2. *Phys. Rev. Lett.* **2001**, *87*, 196803.

(21) Lucking, M. C.; Bang, J.; Terrones, H.; Sun, Y.-Y.; Zhang, S. Multivalency-induced band gap opening at MoS_2 edges. *Chem. Mater.* **2015**, *27*, 3326−3331.

(22) Tongay, S.; Varnoosfaderani, S. S.; Appleton, B. R.; Wu, J.; Hebard, A. F. Magnetic properties of MoS_2: Existence of ferromagnetism. *Appl. Phys. Lett.* **2012**, *101*, 123105.

(23) Li, Y.; Zhou, Z.; Zhang, S.; Chen, Z. MoS_2 Nanoribbons: High Stability and Unusual Electronic and Magnetic Properties. *J. Am. Chem. Soc.* **2008**, *130*, 16739−16744.

(24) Benson, J.; Li, M.; Wang, S.; Wang, P.; Papakonstantinou, P. Electrocatalytic Hydrogen Evolution Reaction on Edges of a Few Layer Molybdenum Disulfide Nanodots. *ACS Appl. Mater. Interfaces* **2015**, *7*, 14113−14122.

(25) Agrawal, A. V.; Kumar, N.; Venkatesan, S.; Zakhidov, A.; Manspeaker, C.; Zhu, Z.; Hernandez, F. R.; Bao, J.; Kumar, M. Controlled Growth of MoS_2 Flakes from in-Plane to Edge-Enriched 3D Network and Their Surface-Energy Studies. *ACS Appl. Nano Mater.* **2018**, *1*, 2356−2367.

(26) Muralikrishna, S.; Manjunath, K.; Samrat, D.; Reddy, V.; Ramakrishnappa, T.; Nagaraju, D. H. Hydrothermal synthesis of 2D

MoS_2 nanosheets for electrocatalytic hydrogen evolution reaction. *RSC Adv.* **2015**, *5*, 89389−89396.
(27) Munkhbat, B.; Yankovich, A. B.; Baranov, D. G.; Verre, R.; Olsson, E.; Shegai, T. O. Transition metal dichalcogenide metamaterials with atomic precision. *Nat. Commun.* **2020**, *11*, 4604.
(28) Park, H.; Lee, J.; Han, G.; AlMutairi, A.; Kim, Y.-H.; Lee, J.; Kim, Y.-M.; Kim, Y. J.; Yoon, Y.; Kim, S. Nano-patterning on multilayer MoS_2 via block copolymer lithography for highly sensitive and responsive phototransistors. *Commun. Mater.* **2021**, *2*, 94.
(29) Bala, A.; Sen, A.; Kim, Y.-H.; Kim, Y.-M.; Gandla, S.; Park, H.; Kim, S. Large-Area MoS_2 Nanosheets with Triangular Nanopore Arrays as Active and Robust Electrocatalysts for Hydrogen Evolution. *J. Phys. Chem. C* **2022**, *126*, 9696−9703.
(30) Huang, Z.; Deng, W.; Zhang, Z.; Zhao, B.; Zhang, H.; Wang, D.; Li, B.; Liu, M.; Huangfu, Y.; Duan, X. Terminal Atom-Controlled Etching of 2D-TMDs. *Adv. Mater.* **2023**, *35*, 2211252.
(31) Danielsen, D. R.; Lyksborg-Andersen, A.; Nielsen, K. E. S.; Jessen, B. S.; Booth, T. J.; Doan, M.-H.; Zhou, Y.; Bøggild, P.; Gammelgaard, L. Super-Resolution Nanolithography of Two-Dimensional Materials by Anisotropic Etching. *ACS Appl. Mater. Interfaces* **2021**, *13*, 41886−41894.
(32) Huang, D.; Choi, J.; Shih, C.-K.; Li, X. Excitons in semiconductor moiré superlattices. *Nat. Nanotechnol.* **2022**, *17*, 227−238.
(33) Yu, H.; Liu, G.-B.; Yao, W. Brightened spin-triplet interlayer excitons and optical selection rules in van der Waals heterobilayers. *2D Mater.* **2018**, *5*, 035021.
(34) Gu, J.; Ma, L.; Liu, S.; Watanabe, K.; Taniguchi, T.; Hone, J. C.; Shan, J.; Mak, K. F. Dipolar excitonic insulator in a moiré lattice. *Nat. Phys.* **2022**, *18*, 395−400.
(35) Shimazaki, Y.; Schwartz, I.; Watanabe, K.; Taniguchi, T.; Kroner, M.; Imamoğlu, A. Strongly correlated electrons and hybrid excitons in a moiré heterostructure. *Nature* **2020**, *580*, 472−477.
(36) Bhowmik, S.; Warner, J. H.; Rajan, A. G. Role of Chemical Etching in the Nucleation of Nanopores in 2D MoS_2: Insights from First-Principles Calculations. *J. Phys. Chem. C* **2023**, *127*, 6873−6883.
(37) Kovalchuk, S.; Kirchhof, J. N.; Bolotin, K. I.; Harats, M. G. Non-Uniform Strain Engineering of 2D Materials. *Isr. J. Chem.* **2022**, *62*, No. e2021001.
(38) Iqbal, M. W.; Shahzad, K.; Akbar, R.; Hussain, G. A review on Raman finger prints of doping and strain effect in TMDCs. *Microelectron. Eng.* **2020**, *219*, 111152.
(39) He, K.; Poole, C.; Mak, K. F.; Shan, J. Experimental Demonstration of Continuous Electronic Structure Tuning via Strain in Atomically Thin MoS_2. *Nano Lett.* **2013**, *13*, 2931−2936.
(40) Li, H.; Tsai, C.; Koh, A. L.; Cai, L.; Contryman, A. W.; Fragapane, A. H.; Zhao, J.; Han, H. S.; Manoharan, H. C.; Abild-Pedersen, F.; et al. Activating and optimizing MoS_2 basal planes for hydrogen evolution through the formation of strained sulphur vacancies. *Nat. Mater.* **2016**, *15*, 48−53.
(41) Liu, K.; Yan, Q.; Chen, M.; Fan, W.; Sun, Y.; Suh, J.; Fu, D.; Lee, S.; Zhou, J.; Tongay, S.; et al. Elastic Properties of Chemical-Vapor-Deposited Monolayer MoS_2, WS_2, and Their Bilayer Heterostructures. *Nano Lett.* **2014**, *14*, 5097−5103.
(42) Tinoco, M.; Maduro, L.; Masaki, M.; Okunishi, E.; Conesa-Boj, S. Strain-Dependent Edge Structures in MoS_2 Layers. *Nano Lett.* **2017**, *17*, 7021−7026.
(43) Castellanos-Gomez, A.; Buscema, M.; Molenaar, R.; Singh, V.; Janssen, L.; van der Zant, H. S. J.; Steele, G. A. Deterministic transfer of two-dimensional materials by all-dry viscoelastic stamping. *2D Mater.* **2014**, *1*, 011002.
(44) Jadczak, J.; Kutrowska-Girzycka, J.; Kapuściński, P.; Huang, Y. S.; Wójs, A.; Bryja, L. Probing of free and localized excitons and trions in atomically thin WSe_2, WS_2, $MoSe_2$ and MoS_2 in photoluminescence and reflectivity experiments. *Nanotechnology* **2017**, *28*, 395702.
(45) Kaspar, P.; Jeyaram, Y.; Jäckel, H.; Foelske, A.; Kötz, R.; Bellini, S. Silicon nitride hardmask fabrication using a cyclic CHF_3-based reactive ion etching process for vertical profile nanostructures. *J. Vac. Sci. Technol. B: Nanotechnol. Microelectron.* **2010**, *28*, 1179−1186.
(46) Sun, J.; Chen, Z.; Zhou, S.; Sun, Y.; Liu, Z.; Chen, C.; Liu, Y.; Sun, Y.; Wang, M.; Xie, S.; et al. Vertical sidewall of silicon nitride mask and smooth surface of etched-silicon simultaneously obtained using CHF_3/O_2 inductively coupled plasma. *Vacuum* **2023**, *207*, 111650.
(47) Wang, S.; Rong, Y.; Fan, Y.; Pacios, M.; Bhaskaran, H.; He, K.; Warner, J. H. Shape Evolution of Monolayer MoS_2 Crystals Grown by Chemical Vapor Deposition. *Chem. Mater.* **2014**, *26*, 6371−6379.
(48) Wulff, G. XXV. Zur Frage der Geschwindigkeit des Wachsthums und der Auflösung der Krystallflächen. *Z. Kristallogr. Cryst. Mater.* **1901**, *34*, 449−530.
(49) Bahl, O. P.; Evans, E. L.; Thomas, J. M. The identification and some properties of point defects and non-basal dislocations in molybdenite surfaces. *Proc. R. Soc. London, Ser. A* **1968**, *306*, 53−65.
(50) Wang, Z.; Li, Q.; Xu, H.; Dahl-Petersen, C.; Yang, Q.; Cheng, D.; Cao, D.; Besenbacher, F.; Lauritsen, J. V.; Helveg, S.; et al. Controllable etching of MoS_2 basal planes for enhanced hydrogen evolution through the formation of active edge sites. *Nano Energy* **2018**, *49*, 634−643.
(51) Yamamoto, M.; Einstein, T. L.; Fuhrer, M. S.; Cullen, W. G. Anisotropic Etching of Atomically Thin MoS_2. *J. Phys. Chem. C* **2013**, *117*, 25643−25649.
(52) Zhou, H.; Yu, F.; Liu, Y.; Zou, X.; Cong, C.; Qiu, C.; Yu, T.; Yan, Z.; Shen, X.; Sun, L.; et al. Thickness-dependent patterning of MoS_2 sheets with well-oriented triangular pits by heating in air. *Nano Res.* **2013**, *6*, 703−711.
(53) Yang, Y.; He, H.; Xian, H.; Xi, J.; Wu, X.; Chen, A.; Zhu, J.; Xu, H. Periodic and non-periodic stacking in molybdenite (MoS_2) revealed by STEM. *Am. Mineral.* **2022**, *107*, 997−1006.
(54) Cevallos, F. A.; Guo, S.; Heo, H.; Scuri, G.; Zhou, Y.; Sung, J.; Taniguchi, T.; Watanabe, K.; Kim, P.; Park, H.; et al. Liquid Salt Transport Growth of Single Crystals of the Layered Dichalcogenides MoS_2 and WS_2. *Cryst. Growth Des.* **2019**, *19*, 5762−5767.
(55) Zhang, X.; Qiao, X.-F.; Shi, W.; Wu, J.-B.; Jiang, D.-S.; Tan, P.-H. Phonon and Raman scattering of two-dimensional transition metal dichalcogenides from monolayer, multilayer to bulk material. *Chem. Soc. Rev.* **2015**, *44*, 2757−2785.
(56) Robinson, B. J.; Giusca, C. E.; Gonzalez, Y. T.; Kay, N. D.; Kazakova, O.; Kolosov, O. V. Structural, optical and electrostatic properties of single and few-layers MoS_2: effect of substrate. *2D Mater.* **2015**, *2*, 015005.
(57) Saito, R.; Tatsumi, Y.; Huang, S.; Ling, X.; Dresselhaus, M. S. Raman spectroscopy of transition metal dichalcogenides. *J. Phys.: Condens. Matter* **2016**, *28*, 353002.
(58) Zhu, C. R.; Wang, G.; Liu, B. L.; Marie, X.; Qiao, X. F.; Zhang, X.; Wu, X. X.; Fan, H.; Tan, P. H.; Amand, T.; et al. Strain tuning of optical emission energy and polarization in monolayer and bilayer MoS_2. *Phys. Rev. B* **2013**, *88*, 121301.
(59) Peng, Z.; Chen, X.; Fan, Y.; Srolovitz, D. J.; Lei, D. Strain engineering of 2D semiconductors and graphene: from strain fields to band-structure tuning and photonic applications. *Light Sci. Appl.* **2020**, *9*, 190.
(60) Li, M.-Y.; Shi, Y.; Cheng, C.-C.; Lu, L.-S.; Lin, Y.-C.; Tang, H.-L.; Tsai, M.-L.; Chu, C.-W.; Wei, K.-H.; He, J.-H.; et al. Epitaxial growth of a monolayer WSe_2-MoS_2 lateral p-n junction with an atomically sharp interface. *Science* **2015**, *349*, 524−528.
(61) Hui, Y. Y.; Liu, X.; Jie, W.; Chan, N. Y.; Hao, J.; Hsu, Y.-T.; Li, L.-J.; Guo, W.; Lau, S. P. Exceptional Tunability of Band Energy in a Compressively Strained Trilayer MoS_2 Sheet. *ACS Nano* **2013**, *7*, 7126−7131 (PMID: 23844893).
(62) Yang, L.; Cui, X.; Zhang, J.; et al. Lattice strain effects on the optical properties of MoS_2 nanosheets. *Sci. Rep.* **2014**, *4*, 5649.
(63) Conley, H. J.; Wang, B.; Ziegler, J. I.; Haglund, R. F. J.; Pantelides, S. T.; Bolotin, K. I. Bandgap Engineering of Strained Monolayer and Bilayer MoS_2. *Nano Lett.* **2013**, *13*, 3626−3630 (PMID: 23819588).

https://doi.org/10.1021/acs.jpcc.3c03812
J. Phys. Chem. C 2023, 127, 15395−15405

(64) Li, H.; Contryman, A. W.; Qian, X.; Ardakani, S. M.; Gong, Y.; Wang, X.; Weisse, J. M.; Lee, C. H.; Zhao, J.; Ajayan, P. M.; et al. Optoelectronic crystal of artificial atoms in strain-textured molybdenum disulphide. *Nat. Commun.* **2015**, *6*, 7381.
(65) Regan, E. C.; Wang, D.; Jin, C.; Utama, M. I. B.; Gao, B.; Wei, X.; Zhao, S.; Zhao, W.; Zhang, Z.; Yumigeta, K.; et al. Mott and generalized Wigner crystal states in WSe_2/WS_2 moiré superlattices. *Nature* **2020**, *579*, 359−363.
(66) Dong, Y.; Yang, M.-M.; Yoshii, M.; Matsuoka, S.; Kitamura, S.; Hasegawa, T.; Ogawa, N.; Morimoto, T.; Ideue, T.; Iwasa, Y. Giant bulk piezophotovoltaic effect in 3R-MoS_2. *Nat. Nanotechnol.* **2023**, *18*, 36−41.
(67) Wen, X.; Gong, Z.; Li, D. Nonlinear optics of two-dimensional transition metal dichalcogenides. *InfoMat* **2019**, *1*, 317−337.
(68) Lin, K.-I.; Ho, Y.-H.; Liu, S.-B.; Ciou, J.-J.; Huang, B.-T.; Chen, C.; Chang, H.-C.; Tu, C.-L.; Chen, C.-H. Atom-Dependent Edge-Enhanced Second-Harmonic Generation on MoS_2 Monolayers. *Nano Lett.* **2018**, *18*, 793−797.
(69) Shree, S.; Lagarde, D.; Lombez, L.; Robert, C.; Balocchi, A.; Watanabe, K.; Taniguchi, T.; Marie, X.; Gerber, I. C.; Glazov, M. M.; et al. Interlayer exciton mediated second harmonic generation in bilayer MoS_2. *Nat. Commun.* **2021**, *12*, 6894.
(70) Mennel, L.; Paur, M.; Mueller, T. Second harmonic generation in strained transition metal dichalcogenide monolayers: MoS_2, $MoSe_2$, WS_2, and WSe_2. *APL Photonics* **2019**, *4*, 034404.
(71) Kumar, N.; Najmaei, S.; Cui, Q.; Ceballos, F.; Ajayan, P. M.; Lou, J.; Zhao, H. Second harmonic microscopy of monolayer MoS_2. *Phys. Rev. B* **2013**, *87*, 161403.
(72) Chen, D.; Lian, Z.; Huang, X.; Su, Y.; Rashetnia, M.; Ma, L.; Yan, L.; Blei, M.; Xiang, L.; Taniguchi, T.; et al. Excitonic insulator in a heterojunction moiré superlattice. *Nat. Phys.* **2022**, *18*, 1171−1176.
(73) Brem, S.; Linderälv, C.; Erhart, P.; Malic, E. Tunable Phases of Moiré Excitons in van der Waals Heterostructures. *Nano Lett.* **2020**, *20*, 8534−8540.
(74) Ling, H.; Li, R.; Davoyan, A. R. All van der Waals Integrated Nanophotonics with Bulk Transition Metal Dichalcogenides. *ACS Photonics* **2021**, *8*, 721−730.
(75) Munkhbat, B.; Küçüköz, B.; Baranov, D. G.; Antosiewicz, T. J.; Shegai, T. O. Nanostructured Transition Metal Dichalcogenide Multilayers for Advanced Nanophotonics. *Laser Photonics Rev.* **2023**, *17*, 2200057.

https://doi.org/10.1021/acs.jpcc.3c03812
J. Phys. Chem. C 2023, 127, 15395−15405